Constraints on 3-D stress in the crust from support of mid-ocean ridge topography

Karen Luttrell[1,2] and David Sandwell[1]

Received 9 August 2011; revised 17 December 2011; accepted 19 February 2012; published 10 April 2012.

[1] The direction of crustal stresses acting at mid-ocean ridges is well characterized, but the magnitude of these stresses is poorly constrained. We present a method by which the absolute magnitude of these stresses may be constrained using seafloor topography and gravity. The topography is divided into a short-wavelength portion, created by rifting, magmatism, and transform faulting, and a long-wavelength portion associated with the cooling and subsidence of the oceanic lithosphere. The short-wavelength surface and Moho topography are used to calculate the spatially varying 3-D stress tensor in the crust by assuming that in creating this topography, the deviatoric stress reached the elastic-plastic limiting stress; the Moho topography is constrained by short-wavelength gravity variations. Under these assumptions, an incompressible elastic material gives the smallest plastic failure stress associated with this topography. This short-wavelength topographic stress generally predicts the wrong style of earthquake focal mechanisms at ridges and transform faults. However, the addition of an in-plane regional stress field is able to reconcile the combined crustal stress with both the ridge and transform focal mechanisms. By adjusting the magnitude of the regional stress, we determine a lower bound for in situ ridge-perpendicular extension of 25–40 MPa along the slow spreading mid-Atlantic ridge, 40–50 MPa along the ultra–slow spreading ridges in the western Indian Ocean, and 10–30 MPa along the fast spreading ridges of the southeastern Indian and Pacific Oceans. Furthermore, we constrain the magnitude of ridge-parallel extension to be between 4 and 8 MPa in the Atlantic Ocean, between −1 and 7 MPa in the western Indian Ocean, and between −1 and 3 MPa in the southeastern Indian and Pacific Oceans. These observations suggest that a deep transform valley is an essential feature of the ridge-transform spreading center.

Citation: Luttrell, K., and D. Sandwell (2012), Constraints on 3-D stress in the crust from support of mid-ocean ridge topography, *J. Geophys. Res.*, *117*, B04402, doi:10.1029/2011JB008765.

1. Introduction

[2] The more than 50,000 km long global mid-ocean ridge is the morphologic result of rifting, magmatism, and transform faulting associated with seafloor spreading driven by plate tectonic forces. The magnitude of the resistive stresses needed to produce spreading and the associated topography is poorly constrained, especially along the remote ocean ridges where in situ stress measurements are largely unavailable [*Heidbach et al.*, 2008]. Bathymetry and gravity are two global data sets that could be used to constrain crustal stress in the spreading environment. To first order, the cross-sectional shape of the spreading axis has either an axial valley or axial high depending on spreading rate and magma supply [*Macdonald*, 1982; *Small and Sandwell*, 1994]. Along slower spreading ridges, the axial valley is often shallower at the center of a ridge segment and systematically deepens toward the adjacent ridge-transform intersections [*Blackman and Forsyth*, 1989]. First-order ridge segments are usually oriented perpendicular to the spreading direction and are offset by transform faults with a characteristic spacing that also depends on spreading rate [*Fox and Gallo*, 1984]. Second-order offsets in some cases overlap and curve toward one another in the overlapping section. Most of these features seem to be spreading rate dependent [e.g., *Chen*, 1992, 1996; *Dick et al.*, 2003; *Purdy et al.*, 1992; *Sandwell and Smith*, 2009; *Small and Sandwell*, 1994].

[3] In regions where adjacent offset ridges are connected by an orthogonal transform fault, that transform often coincides with a deep valley. These deep oceanic transform valleys exhibit some of the steepest topography gradients anywhere on Earth's surface. It has long been the subject of debate whether transform faults at mid-ocean ridges are necessarily inherited structures from the prerifted plate or whether these features can evolve emergently from the processes that incite ridge development [e.g., *Choi et al.*, 2008; *Collette*, 1974; *Gerya*, 2010; *Oldenburg and Brune*, 1972].

[1]Scripps Institution of Oceanography, University of California, San Diego, La Jolla, California, USA.
[2]Now at Volcano Science Center, U. S. Geological Survey, Menlo Park, California, USA.

0148-0227/12/2011JB008765

Though recent studies have been able to identify emergent origins for a ridge-transform spreading morphology, none have reproduced the consistently deep topography of transforms.

[4] While much is known about the orientation of the stress field at mid-ocean ridges, less is known about its magnitude. Primary observations of principal stress axes indicated by focal mechanisms show that the stress field at mid-ocean ridges is primarily 2-D and dominated by ridge-perpendicular extension. However, *Gudmundsson* [1995] showed that various morphological characteristics of ridge-transform systems are better explained when the long-wavelength component of stress at mid-ocean ridges is one of biaxial extension, with both ridge-perpendicular and ridge-parallel stresses, rather than uniaxial extension in the ridge-perpendicular direction alone. Possible origins of this ridge-parallel component include thermal stress [*Choi et al.*, 2008; *Sandwell*, 1986], flexural stress response to changes in spreading direction [*Pockalny et al.*, 1996], and plane stress resulting from isostatic compensation of the long-wavelength topography [*Neves et al.*, 2004]. Several studies have worked to constrain the ratio of ridge-normal stress to transform shear stress using the observations of ridge axis curvature toward a ridge-transform intersection [e.g., *Grindlay and Fox*, 1993; *Phipps Morgan and Parmentier*, 1984], and more recent models have related the ratio of ridge-parallel thermal stress to ridge-perpendicular spreading-induced stress to spreading rate dependent expressions of ridge-transform intersection morphology [*Choi et al.*, 2008]. While these forward-modeling studies help identify and describe the physical mechanisms guiding the evolution of ridge-transform systems, they generally only refer to relative stress quantities and are unable to constrain the absolute magnitude of stress.

[5] The aim of this study is to establish plate boundary-scale absolute constraints on the size of the long-wavelength stress field along the entire global mid-ocean ridge, both the ridge-perpendicular and ridge-parallel components. Generally, lithospheric stress estimates from topography and density variations can be made at three types of length scales. The longest-wavelength estimates assume 2-D lithospheric stress and compute variations at degree scale [e.g., *Coblentz et al.*, 1994; *Ghosh et al.*, 2009]. The shortest-wavelength estimates consider the 3-D surface tractions induced by sloping surface topography [e.g., *Martel and Muller*, 2000]. These consider features at a scale less than 1 km, with the influence to the lithospheric stress field dissipating at a depth comparable to the height of the topographic feature. Our analysis considers topography variations at a scale between these two, estimating the 3-D absolute stress field associated with short-wavelength (~2–300 km) variations in bathymetry, including the ridge crest, median valley, and low transform valley. This estimate assumes that spreading plate boundary topography indicates a plate that is critically strained beyond the plastic limit such that the actual stress state is the minimum deviatoric stress necessary to support the topography [e.g., *Dahlen*, 1981], which is an end-member of the stress in a thick elastic plate loaded by topography. Part of this calculation also involves a global gravity flexure analysis to determine the variation of the elastic thickness parameter along the global mid-ocean ridge and constrain the strength of the brittle oceanic lithosphere.

[6] On the basis of this stress estimate, we may place absolute upper and lower constraints on the magnitude of long-wavelength (>300 km) ridge-parallel stress, whether in compression or extension, and an absolute lower bound on the magnitude of ridge-perpendicular extension. We do this by requiring the total deviatoric stress field along a ridge or transform segment to be in a normal or strike-slip stress regime, respectively, consistent with the observations of earthquake focal mechanisms. The dominant factor in this analysis is the relative depth of the ridge and transform bathymetry across a particular region, but it is also sensitive to other local bathymetric features such as the presence of flanking bathymetric highs and the curvature of spreading segments at ridge-transform intersections.

[7] Through our analysis we find a spreading rate dependence for the long-wavelength stress components such that the strength of the oceanic lithosphere, the magnitude of ridge-parallel extension, and the magnitude of ridge-perpendicular extension are all systematically higher at slower spreading centers and lower at fast spreading centers. Another result of our analysis is the suggestion that the low bathymetry observed at transform zones is a necessary feature of ridge-transform morphology, playing an important part in the mechanics of the region. The absolute magnitude of plate boundary forces has implications for efforts at modeling specific regional processes.

2. Short- and Long-Wavelength Stress at Ridges and Transforms

[8] To first order, a mid-ocean ridge consists of alternating segments of uplifted spreading ridge axis with stress in a normal regime and deep, slipping transforms with stress in a strike-slip regime. If we initially assume that principal axes of the 3-D in situ stress tensor are aligned so that they are approximately vertical σ_V, ridge-perpendicular $\sigma_\perp$, and ridge-parallel $\sigma_\parallel$, then the stress state at the normal ridge axis requires

$$\sigma_V < \sigma_\parallel < \sigma_\perp, \tag{1}$$

while the stress state at the transform offsets requires

$$\sigma_\parallel < \sigma_V < \sigma_\perp, \tag{2}$$

where stress is positive in extension. We then divide the stresses into a short-wavelength topography-related component σ_{topo}, consisting of three principal stresses (σ_{Vtopo}, $\sigma_{\parallel topo}$, and $\sigma_{\perp topo}$), and a long-wavelength plate-driving component $\Delta\sigma$, consisting of two principal stresses ($\Delta\sigma_\parallel$ and $\Delta\sigma_\perp$). At the ridges, these stress components can be related by

$$\sigma_{Vtopo} < \sigma_{\parallel topo} + \Delta\sigma_\parallel < \sigma_{\perp topo} + \Delta\sigma_\perp, \tag{3}$$

while at the transforms

$$\sigma_{\parallel topo} + \Delta\sigma_\parallel < \sigma_{Vtopo} < \sigma_{\perp topo} + \Delta\sigma_\perp. \tag{4}$$

[9] If we then assume the long-wavelength stress components are uniform across adjacent ridge and transform segments, then by calculating the components of short-

wavelength topography stress, we can place the following constraints on the size of the long-wavelength stress components:

$$\left(\sigma_{Vtopo} - \sigma_{\parallel topo}\right)_{ridge} < \Delta\sigma_{\parallel} < \left(\sigma_{Vtopo} - \sigma_{\parallel topo}\right)_{transform}, \quad (5)$$

$$\begin{aligned} \Delta\sigma_{\perp} &> \left(\sigma_{\parallel topo} + \Delta\sigma_{\parallel} - \sigma_{\perp topo}\right)_{ridge} \\ \Delta\sigma_{\perp} &> \left(\sigma_{Vtopo} - \sigma_{\perp topo}\right)_{transform}. \end{aligned} \quad (6)$$

[10] The condition on the ridge-perpendicular stress can always be met by increasing its value. Therefore this analysis can only place a lower bound on ridge-perpendicular stress. The ridge-parallel component, however, is constrained on both sides by the topography stress components at the ridge and transform segments. To first order, we show below that both constraints are satisfied when the depth of the transform valley exceeds the depth of the ridge axis (axial valley or axial high). However, they are also sensitive to other local bathymetric features, such as the presence of flanking bathymetric highs and the curvature of spreading segments, because it is the difference between the vertical and ridge-parallel components of the short-wavelength stress variations that makes up the key constraint.

[11] The first step to estimating these bounding stress values is to divide the in situ stress field in the lithosphere into a short-wavelength component and a long-wavelength component. The unknown long-wavelength portion is composed of all the stresses resulting from plate driving, including ridge push, slab pull, basal traction, etc., and may be safely assumed to be regionally homogeneous over the scale of individual adjacent ridge-transform segments, ~300 km or less. (It is most convenient to consider the lithostatic component of the stress field separately from the deviations from the lithostatic state, and any reference to the total stress field or long-wavelength component of the stress field throughout this study should be interpreted as the total or long-wavelength portion of the nonlithostatic component of the stress field.) The short-wavelength component of the in situ stress field consists of all the local processes of buoyant uplift, failure by brittle faulting or magmatic extension, gradual thermal cooling, etc., that define the individual characteristics of each ridge, transform, or nontransform offset segment, in practicality down to a resolution of ~2 km. Though the long- and short-wavelength physical mechanisms may not be truly independent over geologic time, at a given instant (e.g., the present day) we may calculate their effects independently and superpose them linearly to infer the total in situ stress state.

[12] We assume that the short-wavelength (segment scale or less) variations in the stress field are expressed in the topographic features in the same spectral band, such that the stress field variations at this wavelength may be uniquely identified by the topographic structure. At mid-ocean ridges, the topographic features in this wavelength band include the ridge crests, the axial highs or valleys, the low transform valleys and fracture zones, and the adjacent transform-flanking ridges. These features form over time through a complicated sequence of brittle and plastic deformation events that can be difficult to forward model [e.g., *Buck et al.*, 2005; *Chen*, 1996; *Macdonald et al.*, 1996; *Menard*, 1984; *Pockalny et al.*, 1996]. However, regardless of the exact nature of this deformation, we can reasonably assume that deformation at the active mid-ocean ridge plate boundary has reached a critical plastic limit such that the topography could not be any greater, and any additional applied stress would result in gross plate motion [*Chen and Morgan*, 1990; *Dahlen*, 1981]. We will refer to this stress state as the critical plastic failure stress state.

[13] We can then determine the stress field that is supporting the short-wavelength topography. Assuming it has reached a plastic limit, the height of the topography is set by the depth to the brittle-ductile transition, as only stresses in the brittle portion of the lithosphere will be sustained long-term. In the oceans, this transition is approximately coincident with the 600°C isotherm which, depending on spreading rate and the presence of any hydrothermal cooling processes, may be as shallow as 3 km or as deep as 13 km [e.g., *Gregg et al.*, 2007]. However, the directly on-axis effect of shallow crustal melt, where present, largely diminishes within a few kilometers of the ridge axis leaving a largely solid crust [e.g., *Buck et al.*, 2005; *Crawford et al.*, 1998]. Therefore for the purposes of this study in which the shortest wavelengths considered are ~2 km, the Moho may be considered the approximate depth of compensation for this topography, such that all short-wavelength topography-supporting stress is sustained above this depth. If we assume that oceanic crust deforms according to an elastic-perfectly plastic rheology, then the stress state supporting the observed topography at the critical elastic-plastic transition may be calculated by considering the elastic plate stresses associated with that topography.

[14] We calculate the short-wavelength stress variations from topography within a finite thickness elastic plate that is loaded at its surface and base using a semianalytic model (see Appendix A). In the shortest-wavelength limit, these reduce to those of an elastic half space [e.g., *Martel and Muller*, 2000] and in the longest-wavelength limit they reduce to the solutions of 2-D gravitational potential energy calculations [e.g., *Coblentz et al.*, 1994]. The surface load is the weight of the observed short-wavelength topography, including the weight of the seawater above. The base load is that of the buoyant forces acting at or near the depth of compensation, including principally the compositional buoyancy above the actual Moho but also including any thermal buoyancy acting at these scales. As a force balance problem, the weight of the surface topography must be supported either by the buoyancy at the depth of the Moho or by the strength of the oceanic crust. For plastic failure, the critical quantity is the second invariant of the deviatoric stress tensor, sometimes known as the Von Mises stress. For an elastic stress state, this invariant quantity depends only on the applied loads and the Poisson's ratio of the material. A material with a Poisson's ratio of 0.5, corresponding to an incompressible elastic solid, has the smallest possible Von Mises stress associated with a given load [*Luttrell et al.*, 2011]. Because we intend to establish firm constraints on the absolute magnitude of the in situ stress state at the mid-ocean ridge, we proceed by calculating the stress state in an incompressible material so that the lower bounds we calculate may be taken as an absolute minimum.

[15] We can then use the pattern of local stress variations to determine constraints on the size of the long-wavelength stresses, as in equations (5) and (6). Figure 1 illustrates this

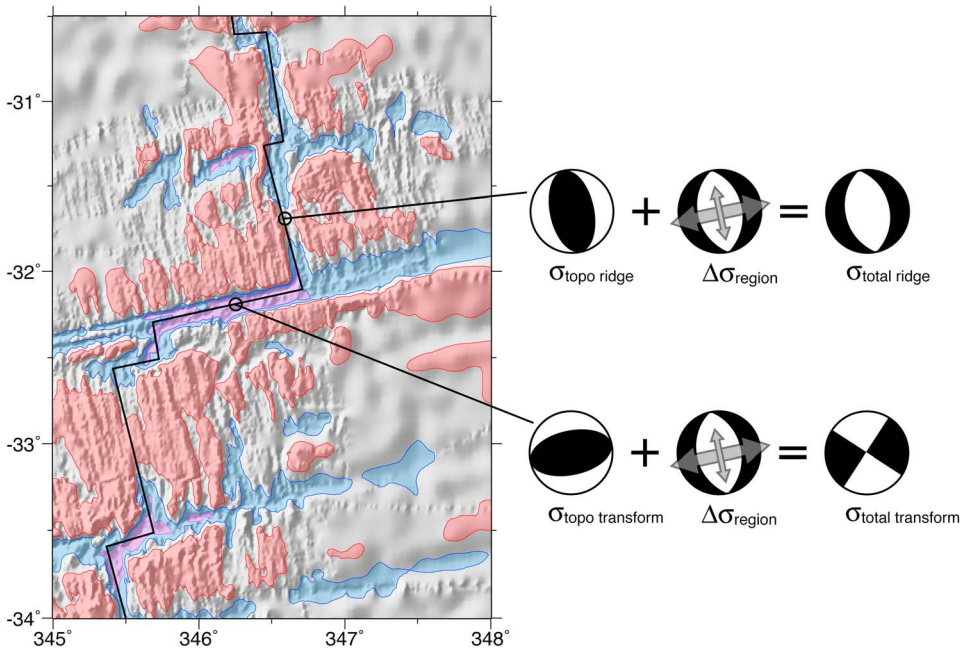

Figure 1. Schematic of short- and long-wavelength stress orientations at mid-ocean ridge and transform segments. Gray shaded bathymetry shown for a small region of the South Atlantic (within subregion 4b in Figure 2). Contours of high-pass-filtered bathymetry are shown as shaded regions, with red, blue, and purple indicating high, low, and very low regions, respectively. Contour interval is 300 m. Black line indicates the plate boundary. Schematic focal mechanisms illustrate the individual orientations of short- and long-wavelength stress components, as well as the total stress at both ridge and transform segments.

schematically. The gray shaded bathymetry shown is from a region of the southern mid-Atlantic ridge. The colored regions are defined by contours of high-pass-filtered bathymetry at a 300 m interval, such that the high red regions are at least 300 m above the low blue regions and at least 600 m above the very low purple regions. At both the low ridge axis and transform valley, the stress state from topography would be in a thrust regime with orientation determined by the geometry of the adjacent high topography. The long-wavelength stress across the entire region is approximately one of ridge-perpendicular extension with a normal regime. This extension must be large enough that the total regime at the ridge axis is normal, but not so large that the total regime at the transform also becomes normal.

3. Methods

[16] We begin by identifying the wavelengths of topography that can be related to the stress state in the crust. We high-pass filter 1 arc minute bathymetry [*Becker et al.*, 2009; *Smith and Sandwell*, 1997] and 1 arc minute gravity data [*Sandwell and Smith*, 2009] between spherical harmonics 100 and 140, corresponding to wavelengths between 300 and 400 km. This is long enough to include all the flexural features of the lithosphere, but short enough to remove the effects of any deep mantle processes. We then determine the best single depth location and approximate shape of the buoyant load at the depth of compensation by calculating the gravity field from a plate whose base load is related to the surface load through flexure (Appendix B) [*Watts*, 2001]. Modeled gravity is then compared to gravity observations at locations that are both within 30 km of the plate boundary and where bathymetry data are from ship soundings, to ensure the compared gravity fields are derived from independent data. We identify the optimal regional values of crustal density and elastic thickness for each spreading plate boundary individually, as well as for several plate subregions divided on the basis of spreading behavior (Figure 2 and Table 1).

[17] Using these regional parameters, we estimate the spatial variation in the 3-D stress field by calculating the stress tensor throughout a thick elastic plate loaded by high-pass-filtered bathymetry on the surface and by the corresponding deformed buoyant short-wavelength Moho at 7 km depth. The six components of the 3-D stress tensor are calculated using a semianalytic model consisting of an analytically derived Green's function for surface point loads convolved with the actual 2-D shape of the loads (Appendix A). We then integrate the stress components over the plate depth. This has two effects. First it provides a number that can be mathematically added to 2-D depth averaged stress field from longer-wavelength sources. Second, the influence of the unphysically large bending stresses and vertical shear stresses present within ~1 km of the surfaces of a thin but mathematically finite plate are greatly reduced, leaving a stress estimate that is primarily influenced by the loading and bending associated with the bathymetry-related features we are primarily interested in.

[18] We calculate the plastic failure stress associated with the sustained topography as the square root of the second

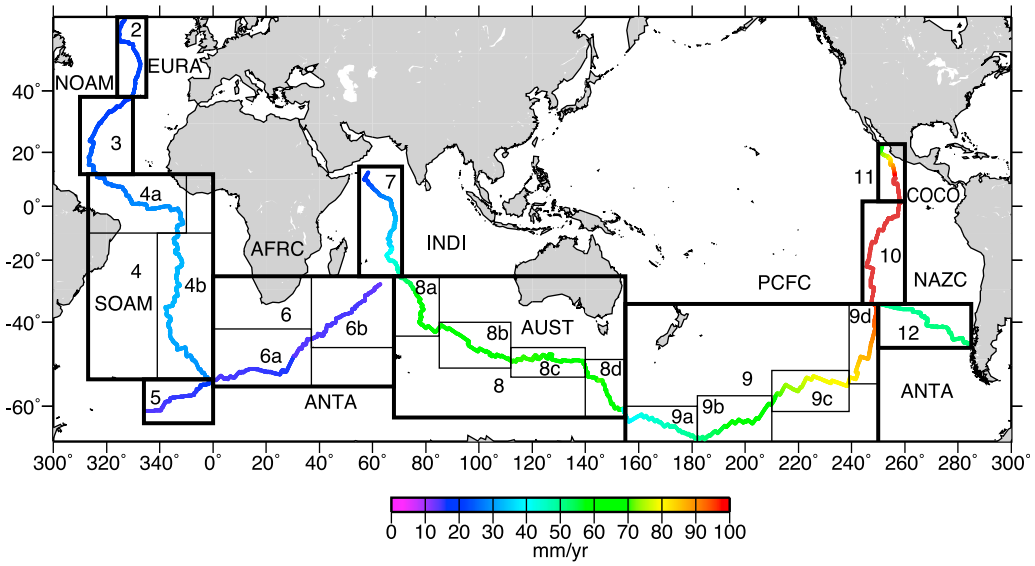

Figure 2. Spreading rate along the global mid-ocean ridge [*DeMets et al.*, 2010] and plate boundaries and subregions considered in this study. The numbers in each box correspond to the regions listed in Tables 1 and 3. Labels correspond to major tectonic plates: NOAM, North American; EURA, Eurasian; SOAM, South American; AFRC, African; ANTA, Antarctic; INDI, Indian; AUST, Australian; PCFC, Pacific; NAZC, Nazca; and COCO, Cocos.

invariant of the deviatoric component of this depth averaged stress tensor (Von Mises stress). This critical plastic failure stress ranges from near zero in the flattest least-deformed regions (e.g., along the East Pacific Rise) to about 70 MPa in the steepest regions along deep transform valleys (e.g., the Romanche or Udintsev valleys), where the deviatoric stress must be quite large to sustain the high load gradient. Figure 3a shows the critical plastic failure stress in a region of the southern mid-Atlantic ridge. Failure stress is ~25 MPa in the deep narrow transform valley, 15–20 MPa at the ridge-transform intersections, and 5–10 MPa along the spreading ridge axis.

[19] These depth-averaged short-wavelength variations in the stress field are used to constrain the magnitude of the

Table 1. Gravity RMS, Elastic Thickness, and Crustal Density Values at Each Plate Boundary and Subregion

Number in Figure 2	Plate Boundary	Best T_e (km)	Best ρ_c (kg/m^3)	Best RMS (mGal)	Acceptable T_e (km)	RMS of Acceptable T_e and ρ_c (mGal)	Spreading Rate[a] (mm/yr)
1	Whole earth	5	3000	8.767	6	9.052	—
2[b]	NOAM-EURA	10	2800	11.312	5	11.417	21.7
3	NOAM-AFRC	5	2900	9.381	5	9.515	22.8
4	SOAM-AFRC	5	3000	9.239	6	9.721	30.3
4a	SOAM-AFRC 1	8	2900	9.687	8	9.994	28.4
4b	SOAM-AFRC 2	3	3000	8.151	4	8.811	31.8
5[b]	SOAM-ANTA	4	3000	12.269	5	13.257	15.3
6	AFRC-ANTA	6	3000	14.854	7	16.278	14.7
6a	AFRC-ANTA 1	7	3000	14.938	8	16.530	15.1
6b	AFRC-ANTA 2	5	3000	14.339	6	14.953	14.4
7	AFRC-INDI	8	2900	11.776	7	11.955	33.1
8	AUST-ANTA	2	3000	5.025	3	5.214	65.9
8a	AUST-ANTA 1	2	3000	6.316	2	6.528	58.8
8b	AUST-ANTA 2	2	3000	3.789	3	3.890	68.1
8c	AUST-ANTA 3	2	3000	5.304	3	5.605	69.9
8d[b]	AUST-ANTA 4	2	2900	4.168	2	4.216	66.5
9	PCFC-ANTA	3	3000	6.114	5	6.332	67.6
9a[b]	PCFC-ANTA 1	5	2700	11.485	3	11.572	46.4
9b	PCFC-ANTA 2	2	2900	3.658	2	3.733	59.2
9c	PCFC-ANTA 3	4	3000	7.524	5	7.974	76.2
9d	PCFC-ANTA 4	2	2800	4.679	2	4.679	88.5
10	PCFC-NAZC	3	2700	3.455	2	3.493	137.5
11	PCFC-COCO	11	2600	6.067	8	6.302	92.8
12	NAZC-ANTA	3	3000	8.571	4	8.749	50.7

[a]Spreading rate calculated from Mid-Ocean Ridge Velocity (MORVEL) plate velocities [*DeMets et al.*, 2010].
[b]Denotes regions with few independently constrained gravity and bathymetry points at the plate boundary.

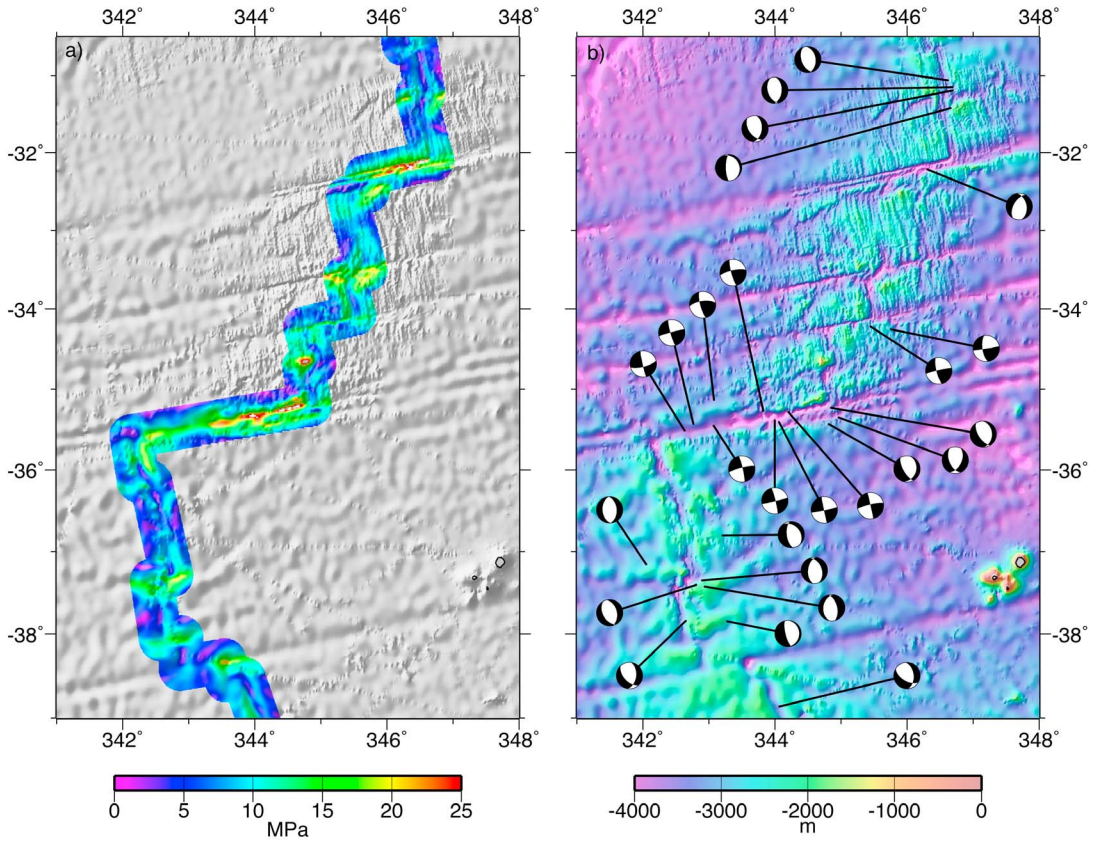

Figure 3. (a) Smallest plastic failure stress associated with short-wavelength topography, measured by the square root of the second invariant of the deviatoric stress field. (b) Bathymetry along a portion of the southern mid-Atlantic ridge (within subregion 4b in Figure 2) with focal mechanisms from the World Stress Map (WSM) catalog [*Heidbach et al.*, 2008].

total stress field. We add a spatially uniform horizontal 2-D stress field to the bathymetry-supporting stress field and determine, on a 1 arc minute grid, the stress regime at each point, defined as in the World Stress Map project [*Zoback*, 1992] by the relative plunge angles of the principal stress axes (Table 2). We consider two sources of observations of the stress regime along the mid-ocean ridge. In the first, we assume that the appropriate regime along the entire length of every spreading ridge axis segment is normal, while the appropriate regime along all offset transform segments is strike slip. The endpoints of each ridge and transform segment are digitized from gravity and bathymetry data [*Sandwell and Smith*, 2009] and the sample locations along each segment are interpolated at a regular interval (~10 km), resulting in ~8000 observations of stress regime evenly sampling the entire mid-ocean ridge. The clear advantage of this data set is that it gives a complete and uniform sampling of the global mid-ocean ridge. The disadvantage is that it a priori presumes the stress regime on the basis of a morphology that requires some subjective judgment to define. We quantitatively define the fit between the regimes of a modeled stress field and the observed stress regimes with a goodness of fit parameter $\xi \in [0, 1]$:

$$\xi = \begin{cases} 1 & \text{if model and observation stress regimes match} \\ 0.25 & \text{if observed stress regime is strikeslip and model stress regime is oblique normal/strike} - \text{slip} \\ 0 & \text{else} \end{cases}. \tag{7}$$

[20] The second observation set we consider is the information in the World Stress Map (WSM) catalog [*Heidbach*

Table 2. World Stress Map Regime Assignment Criteria After *Zoback* [1992]

Regime	Plunge ϕ of Pressure Axis	Plunge ϕ of Intermediate Axis	Plunge ϕ of Tension Axis
Normal	$\phi > 52°$		$\phi < 35°$
Oblique normal/strike slip	$40° < \phi < 52°$		$\phi < 20°$
Strike slip	$\phi < 40°$	$\phi > 45°$	$\phi < 20°$
	$\phi < 20°$	$\phi > 45°$	$\phi < 40°$
Oblique thrust/strike slip	$\phi < 20°$		$40° < \phi < 52°$
Thrust	$\phi < 35°$		$\phi > 52°$
Undefined	any other configuration	any other configuration	any other configuration

et al., 2008]. Along the mid-ocean ridge, this consists of 881 earthquake focal mechanisms, a subset of which is shown in Figure 3b. The advantage of this data set is that it is based on observations of a direct in situ stress-related event (earthquake) rather than a presumed in situ stress-related process (deformation and formation of the ridge axis). Another advantage is that it includes information on the full 3-D orientation of the stress field, and can thus better constrain our calculations. The first major disadvantage is that the observations are not evenly distributed: slow spreading regions tend to have many more large earthquakes than faster-spreading regions. The second major disadvantage is that because the observations are located using seismic waves at stations far away from the events, they are subject to a mislocation error of up to 20–40 km [*Pan et al.*, 2002]. This mislocation is large enough that, for example, a strike-slip earthquake that occurred on a transform valley could appear to be located off the plate boundary where the stress regime may be quite different. Because of these key limitations, we restrict our use of the WSM focal mechanisms to qualitative comparison and rely on the assigned ridge-transform stress regime for quantitative constraints.

[21] The additional 2-D stress is defined by three parameters: the two perpendicular principal stresses and the orientation angle of those stresses. Initially we allowed the orientation angle to vary freely, but found no evidence that an orientation other than ridge-perpendicular and ridge-parallel was warranted. For the remainder of the analysis, we therefore focus on constraining the magnitude of long-wavelength stress aligned with the spreading direction at each point, defined by the Mid-Ocean Ridge Velocity (MORVEL) plate motions [*DeMets et al.*, 2010].

[22] For each candidate long-wavelength stress field, we define a value of ξ at each point along the plate boundary and take the average value at all the ridges or transforms within a region or subregion separately, to get $\bar{\xi}_{ridge}$ and $\bar{\xi}_{transform}$. We then average these two values to get $\bar{\xi}$, the parameter of fit for each region. This averaging is important because the true constraint on the size of the long-wavelength stress depends upon the simultaneous fitting of both ridge and transform data. Averaging the fits to each individually adjusts for a region having a disproportionate quantity of ridge or transform observations.

4. Results

[23] Figure 4 shows contours of the mean fit $\bar{\xi}$ at each plate boundary and subregion as a function of the long-wavelength ridge-perpendicular and ridge-parallel stresses ($\Delta\sigma_\perp$ and $\Delta\sigma_\parallel$). At most of the regions, there is an easily discernable maximum $\bar{\xi}$ contour with a defined minimum ridge-perpendicular value and defined minimum and maximum ridge-parallel values. Because the constraint on $\Delta\sigma_\perp$ depends upon the determined value for $\Delta\sigma_\parallel$ (equation (6)), we first determine the constraint on $\Delta\sigma_\parallel$. This is done by examining a profile of $\bar{\xi}$ versus $\Delta\sigma_\parallel$ at an arbitrarily large value of $\Delta\sigma_\perp$ such that the maximum value of $\bar{\xi}$ is captured, in this case $\Delta\sigma_\perp$ = 100 MPa (Figure 5). For each region, the blue and green curves show the value of ξ averaged over all the ridges and transforms, respectively, within that region. In most regions, some ridge-parallel extension is required to bring all the ridge points in to a normal stress regime. This is an effect of the deep median valleys at some ridge segments, evidenced by the stronger need for ridge-parallel extension at slower spreading regions like AFRC-ANTA than at faster spreading regions like PCFC-NAZC. In the absence of any ridge-parallel stress, most regions fit at least half of the defined transform points, with successively more being fit as ridge-parallel stress becomes more compressive.

[24] The true test of our model is its ability to simultaneously accurately predict regions of ridge normal and transform strike-slip stress regimes. The red line in Figure 5 is the average of $\bar{\xi}_{ridge}$ and $\bar{\xi}_{transform}$, which weights the ridge and transform fits evenly and compensates for any regional difference in the relative abundance of ridge or transform segments. In most regions this curve reaches a clear broad maximum value $\bar{\xi}_{\max}$ somewhere in the range of 0–10 MPa ridge-parallel extension. We define the width of this maximum as the range of $\Delta\sigma_\parallel$ values for which $\bar{\xi} > 0.98\bar{\xi}_{\max}$. This threshold is indicated by the horizontal black line, and the satisfying $\Delta\sigma_\parallel$ range is indicated by the vertical black lines capped with right- and left-pointing arrows. The values of $\Delta\sigma_\parallel$ and $\bar{\xi}_{\max}$ for each plate boundary and subregion are listed in Table 3. In most regions, $\Delta\sigma_\parallel$ is constrained to a narrow range of slightly extensional stress values. In three regions, AFRC-INDI, AUST-ANTA, and AUST-ANTA 4 (regions 7, 8, and 8d), $\bar{\xi}_{\max}$ is 0.550 or below, indicating that in these regions there is no single long-wavelength stress that can be added to our calculated topographic stress and satisfactorily simultaneously fit the expected regime of both ridge and transform regions. Because the models fail in these regions, they are subsequently omitted from the rest of the analysis. The only region which requires ridge-parallel compression is AUST-ANTA 3 (region 8c), consisting of the intermediate-fast spreading discordant section of the plate boundary.

[25] Once the values of $\Delta\sigma_\parallel$ have been determined, we can evaluate profiles of $\bar{\xi}$ versus $\Delta\sigma_\perp$ at the best value of $\Delta\sigma_\parallel$ for each region. In Figure 6, the blue and green lines again show profiles of $\bar{\xi}_{ridge}$ and $\bar{\xi}_{transform}$ respectively, and the red line shows their average. Generally, $\bar{\xi}$ increases rapidly with $\Delta\sigma_\perp$ up to a point, after which it tapers to a maintained maximum level $\bar{\xi}_{\max}$. Once again we define the threshold for determining the value of $\Delta\sigma_\perp$ such that $\bar{\xi} > 0.98\bar{\xi}_{\max}$, indicated by the horizontal black line in each region subplot. The vertical black line with right-pointing triangle end caps indicates the minimum $\Delta\sigma_\perp$ value at which this threshold is reached (values summarized in Table 3). In general, ridge-perpendicular extension must be at least 5–50 MPa to simultaneously fit the regime at both ridges and transforms.

[26] The constrained values of $\bar{\xi}_{\max}$, $\Delta\sigma_\perp$, and $\Delta\sigma_\parallel$ are summarized in Figure 7. Examining these results, we notice a relationship between the constrained stress magnitude and spreading rate. The slower spreading mid-Atlantic segments generally require 4–8 MPa ridge-parallel extension, while the faster-spreading Pacific segments generally require 0–3 MPa ridge-parallel extension, or even slight compression. Once again we notice the unusual result of the discordant zone of AUST-ANTA 3 requiring 2–7 MPa ridge-parallel compression. Constraints on the ridge-perpendicular component

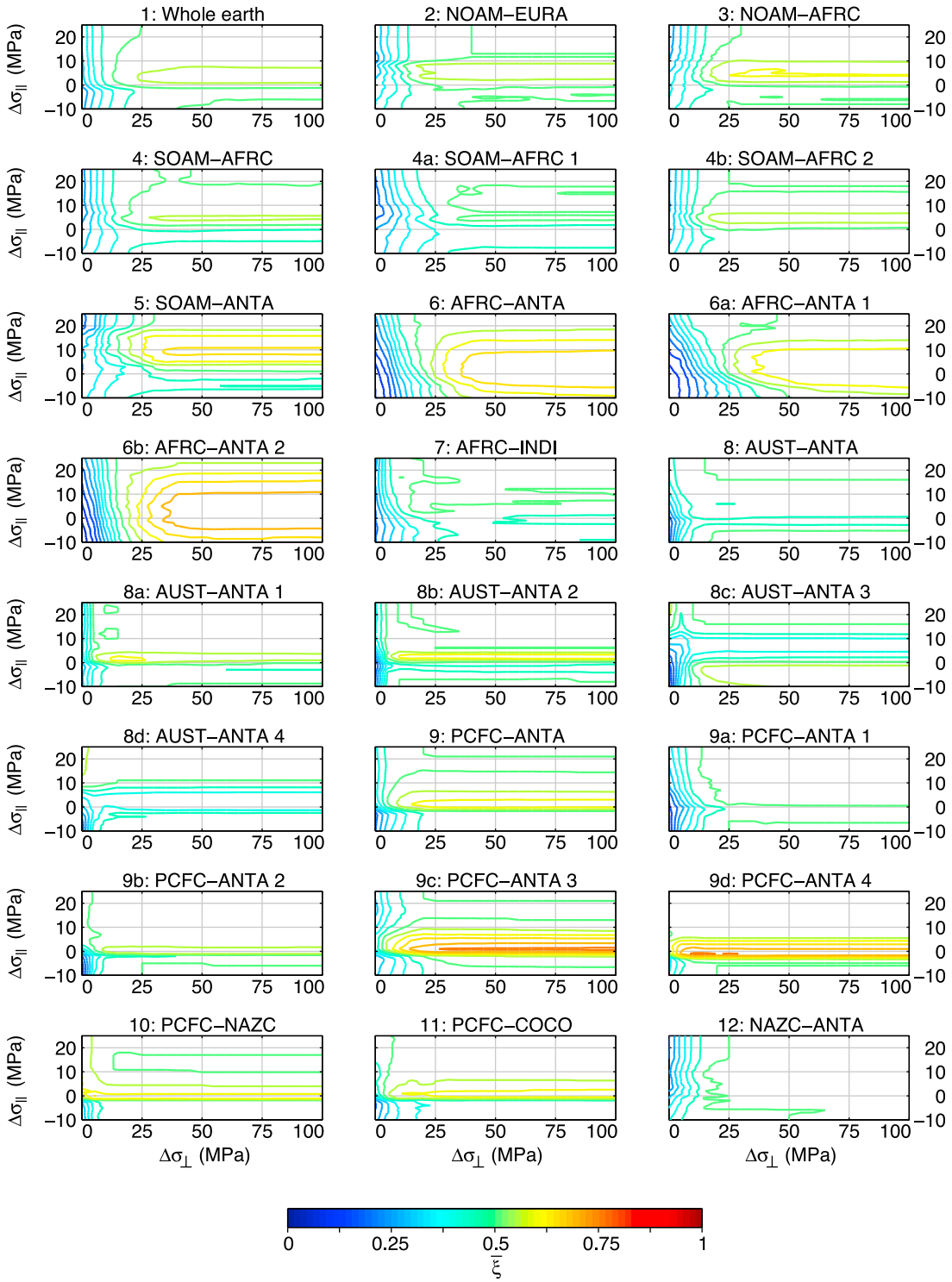

Figure 4. Contours of mean model fit at both ridges and transforms ($\bar{\xi}$) as a function of added ridge-perpendicular and ridge-parallel stress ($\Delta\sigma_\perp$ and $\Delta\sigma_\parallel$, respectively) for each plate boundary and subregion. Contour interval is 0.05. Quantitative fit is defined as in equation (7). Constrained values of $\Delta\sigma_\perp$, $\Delta\sigma_\parallel$, and $\bar{\xi}_{max}$ for each region are summarized in Table 3 and Figure 7.

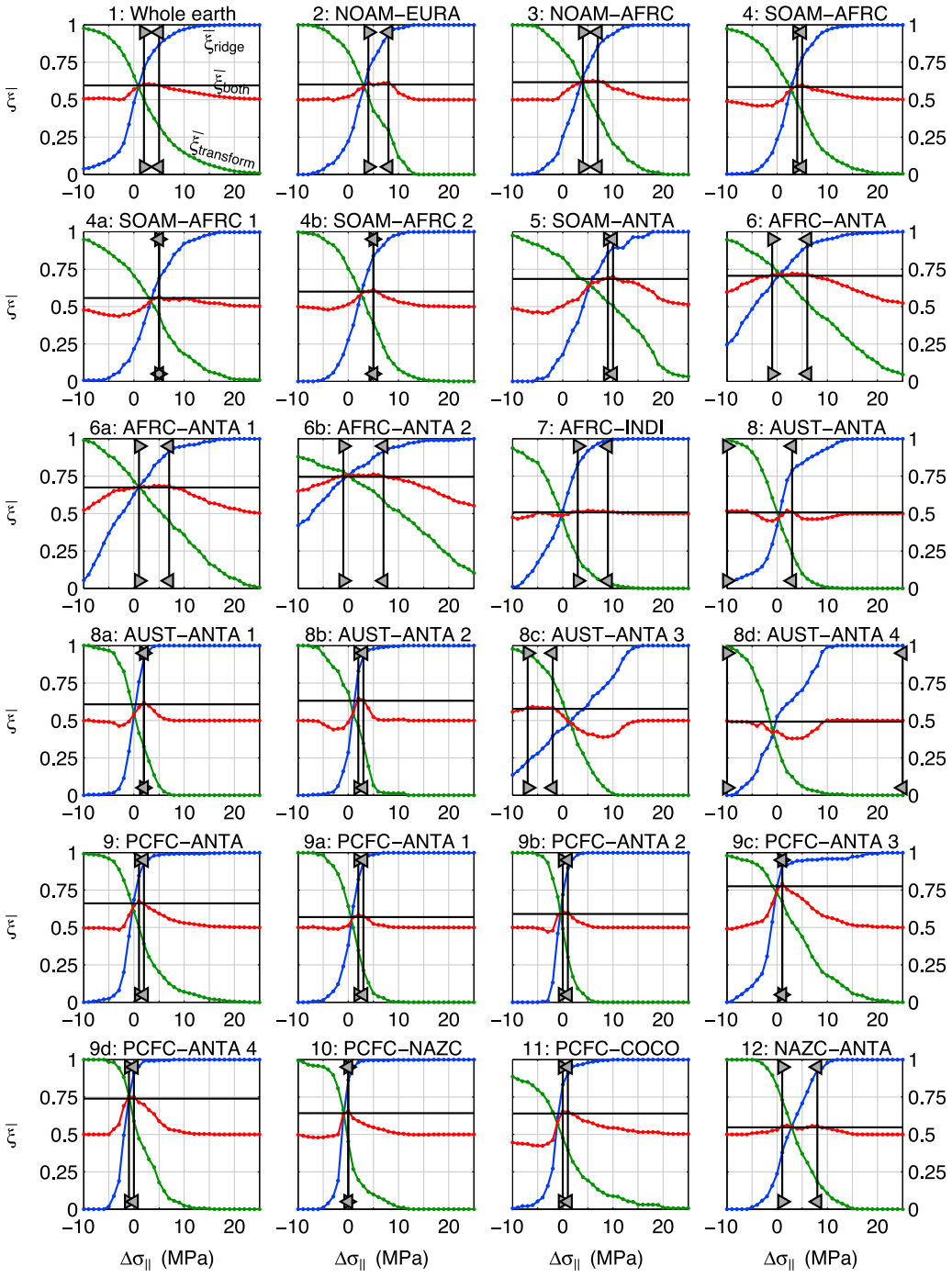

Figure 5. Mean model fit at ridges (blue), transforms (green), and both (red) over each plate boundary and subregion as a function of long-wavelength ridge-parallel stress ($\Delta\sigma_{\parallel}$), assuming a ridge-perpendicular extension of 100 MPa. Horizontal black line indicates the threshold value for determining the range of best fitting stress, $0.98\bar{\xi}_{max}$. Vertical lines capped with right- and left-pointing arrows indicate the minimum and maximum value of $\Delta\sigma_{\parallel}$ that optimizes model fit at both ridges and transforms.

Table 3. Best Mean Model Fit, With Corresponding Range of Long-Wavelength Ridge-Parallel Stress and Minimum Ridge-Perpendicular Stress

Number in Figure 2	Plate Boundary	$\bar{\xi}_{max}$	$\Delta\sigma_{\parallel}$ (MPa)	$\Delta\sigma_{\perp}$ (MPa)
1	Whole earth	0.606	2–5	35
2	NOAM-EURA	0.619	4–8	25
3	NOAM-AFRC	0.638	4–7	25
4	SOAM-AFRC	0.602	4–5	35
4a	SOAM-AFRC 1	0.569	5	40
4b	SOAM-AFRC 2	0.616	5	25
5	SOAM-ANTA	0.701	9–10	40
6	AFRC-ANTA	0.723	−1–6	50
6a	AFRC-ANTA 1	0.686	1–7	50
6b	AFRC-ANTA 2	0.762	−1–7	45
7[a]	AFRC-INDI	0.536	3–9[a]	15[a]
8[a]	AUST-ANTA	0.521	−10–3[a]	15[a]
8a	AUST-ANTA 1	0.643	2	15
8b	AUST-ANTA 2	0.651	2–3	15
8c	AUST-ANTA 3	0.592	−7– −2	35
8d[a]	AUST-ANTA 4	0.541	−10–25[a]	0[a]
9	PCFC-ANTA	0.673	1–2	35
9a	PCFC-ANTA 1	0.583	2–3	40
9b	PCFC-ANTA 2	0.625	0–1	15
9c	PCFC-ANTA 3	0.793	1	30
9d	PCFC-ANTA 4	0.770	−1–0	10
10	PCFC-NAZC	0.670	0	5
11	PCFC-COCO	0.654	0–1	30
12	NAZC-ANTA	0.563	1–8	20

[a]Denotes regions with $\bar{\xi}_{max} < 0.550$, such that constraints on $\Delta\sigma_{\parallel}$ and $\Delta\sigma_{\perp}$ are unreliable.

are somewhat more varied. The slow spreading Atlantic segments require at least 25–40 MPa ridge-perpendicular extension and the ultra–slow spreading regions of the AFRC-ANTA plate boundary require at least 45–50 MPa extension. The faster-spreading Pacific segments are more varied, requiring 5–40 MPa ridge-perpendicular extension.

[27] Figure 8 clarifies the relationship between spreading rate and elastic thickness, $\Delta\sigma_{\perp}$, and $\Delta\sigma_{\parallel}$. A clear decrease in elastic thickness is observed with spreading rate down to ~2 km at 70 mm/yr, after which the dependence tapers off, such that the fastest spreading regions still maintain finite strength with a 2 km elastic thickness. One exception seems to be the 8 km elastic thickness predicted for the PCFC-COCO plate boundary. The ridge-parallel stress shows a similar pattern of decreasing with spreading rate up to about 80 mm/yr, and then leveling off around 0 MPa for faster spreading regions. In this case, the clear exception is again the strong compression required by the discordant zone in the Southern Ocean. The trend is less pronounced for ridge-perpendicular stress, but it still shows a steady decrease in minimum $\Delta\sigma_{\perp}$ value through 90 mm/yr.

[28] It is illustrative to examine the predicted stress regime along the plate boundary in map view. Figure 9 shows the predicted stress regime for the same small region of the southern mid-Atlantic ridge as in Figure 3 computed from short-wavelength topography plus a range of long-wavelength tectonic stress fields. Regime is color coded with blue and yellow indicating normal and strike-slip regimes, red indicating thrust regime, green and orange indicating oblique normal and oblique thrust regimes, and black indicating a regime unable to be classified by the criteria in Table 2. For topography stress alone (Figure 9a), the lowest regions are in a thrust or strike-slip regime, while much of the flanking seafloor is in an unclassifiable orientation. This is due to the large vertical shear stresses associated with a bending plate. As $\Delta\sigma_{\perp}$ increases, the slightly off-axis regions attain a normal regime, but the predicted strike-slip regime is still too widespread (Figure 9c). As $\Delta\sigma_{\parallel}$ increases, the ridges become more consistently normal until an optimal balance is found between a normal regime at the ridge axes and a strike-slip regime at the transform valleys, flanked by narrow transitional regions of oblique normal-strike-slip regime (Figure 9e). As $\Delta\sigma_{\parallel}$ continues to increase, the entire region is moved into a normal regime (Figure 9f).

5. Discussion

[29] Several studies have used numerical models to identify the processes required to initiate new plate spreading and form the pattern of mostly perpendicular ridge and transform segments observed throughout the modern ocean [*Choi et al.*, 2008; *Gerya*, 2010; *Hieronymus*, 2004]. However, though such models can reproduce the characteristic segment spacing and spreading rates associated with various types of plate spreading, including the uplifted topography of ridge flanks, they less consistently reproduce the bathymetric lows of the transform offsets. The stress analysis presented here suggests that a low transform valley relative to the adjacent ridges is an important contributor to the observed stress state. This suggests that transform valleys may not necessarily be an important part of spreading initiation, but rather may play an important role in maintaining a transform offset once initiated. It could be that as a ridge-transform system is developing, those proto-offsets that coincide with deep bathymetry, either inherited or formed by any active inelastic deformation process at that time, are the offsets that persevere, while those whose formation does not coincide with a bathymetric valley are preferentially abandoned. Thus bathymetric valleys, though not necessarily present at the initiation of plate spreading, may be an important part of the development of a mature ridge-spreading system.

[30] Because this analysis focuses on driving-stress estimates at the plate-boundary scale, there are numerous features of mid-ocean ridges that are not specifically included in this analysis. These include hot spots and nontransform offsets, which could perturb the in situ stress field such that it is not solely in a normal regime at ridges and in a strike-slip regime at offsets. Particularly at nontransform offsets, the stress field may include areas of both a strike-slip and normal stress regime whose extents may change over time [e.g., *Grindlay and Fox*, 1993]. If a given nontransform offset is dominantly characterized by an extensional stress regime, then the constraints established by this analysis may be inaccurate at that particular location, particularly the ridge-parallel bounds. However, provided the majority of offsets over a given plate boundary are nontransform, the calculated constraints should still be accurate to first order across the plate boundary.

[31] Though the calculations presented here do not account for preexisting fault structures, the orientation of the fault planes at the normal ridge axis align with the planes of maximum shear stress of the predicted 3-D stress tensor. However, the predicted planes of maximum shear stress at transform offsets, even though the regime is strike slip, strike 45° away from the observed transform. The

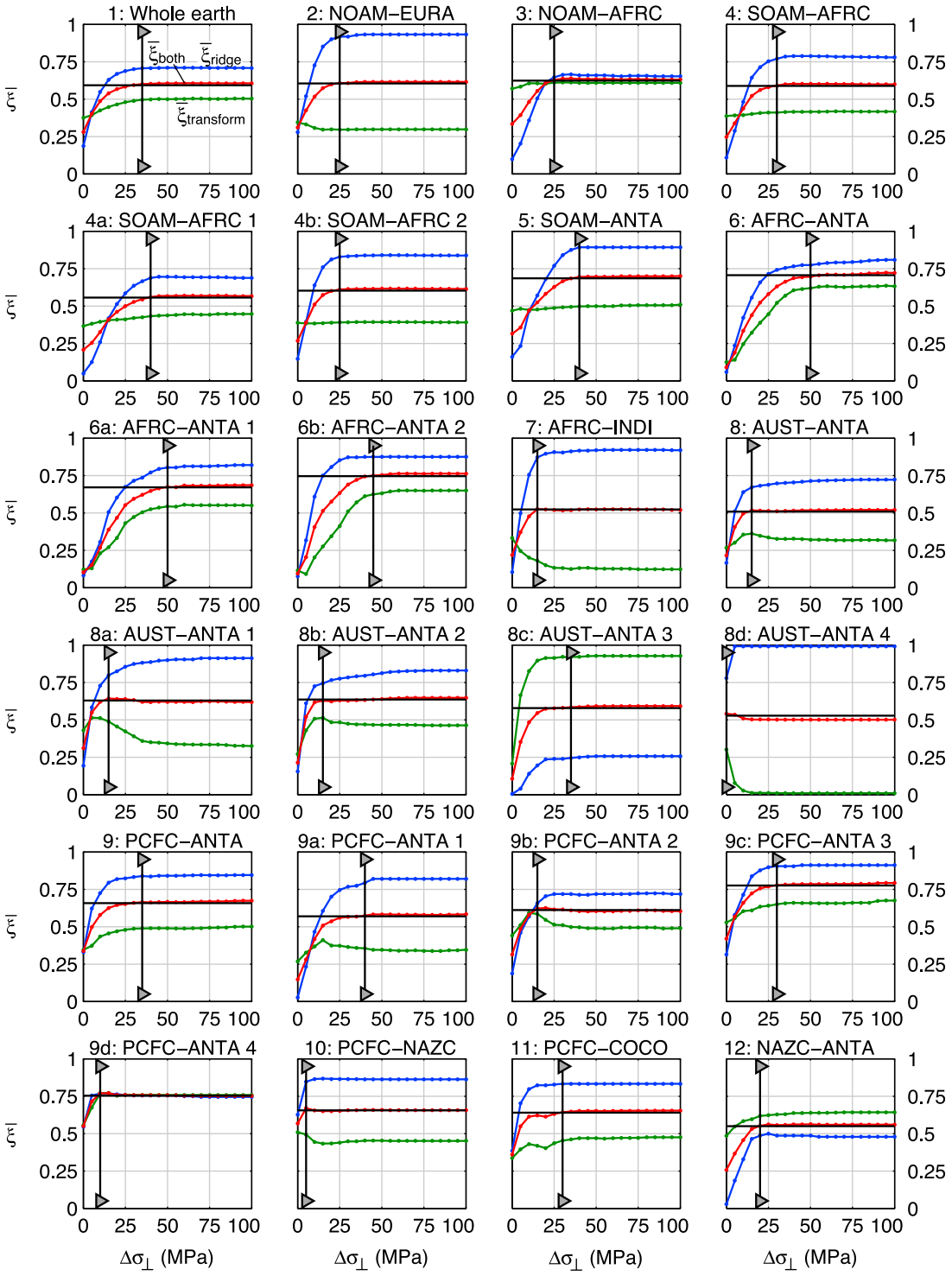

Figure 6. Mean model fit at ridges (blue), transforms (green), and both (red) over each plate boundary and subregion as a function of long-wavelength ridge-perpendicular stress ($\Delta\sigma_\perp$), assuming the optimal ridge-parallel extension value in each region, listed in Table 3. Horizontal black line indicates the threshold value for determining the minimum ridge-perpendicular stress, $0.98\bar{\xi}_{max}$. Vertical line capped with right-pointing arrows indicates the minimum value of $\Delta\sigma_\perp$ that optimizes the fit at both ridges and transforms.

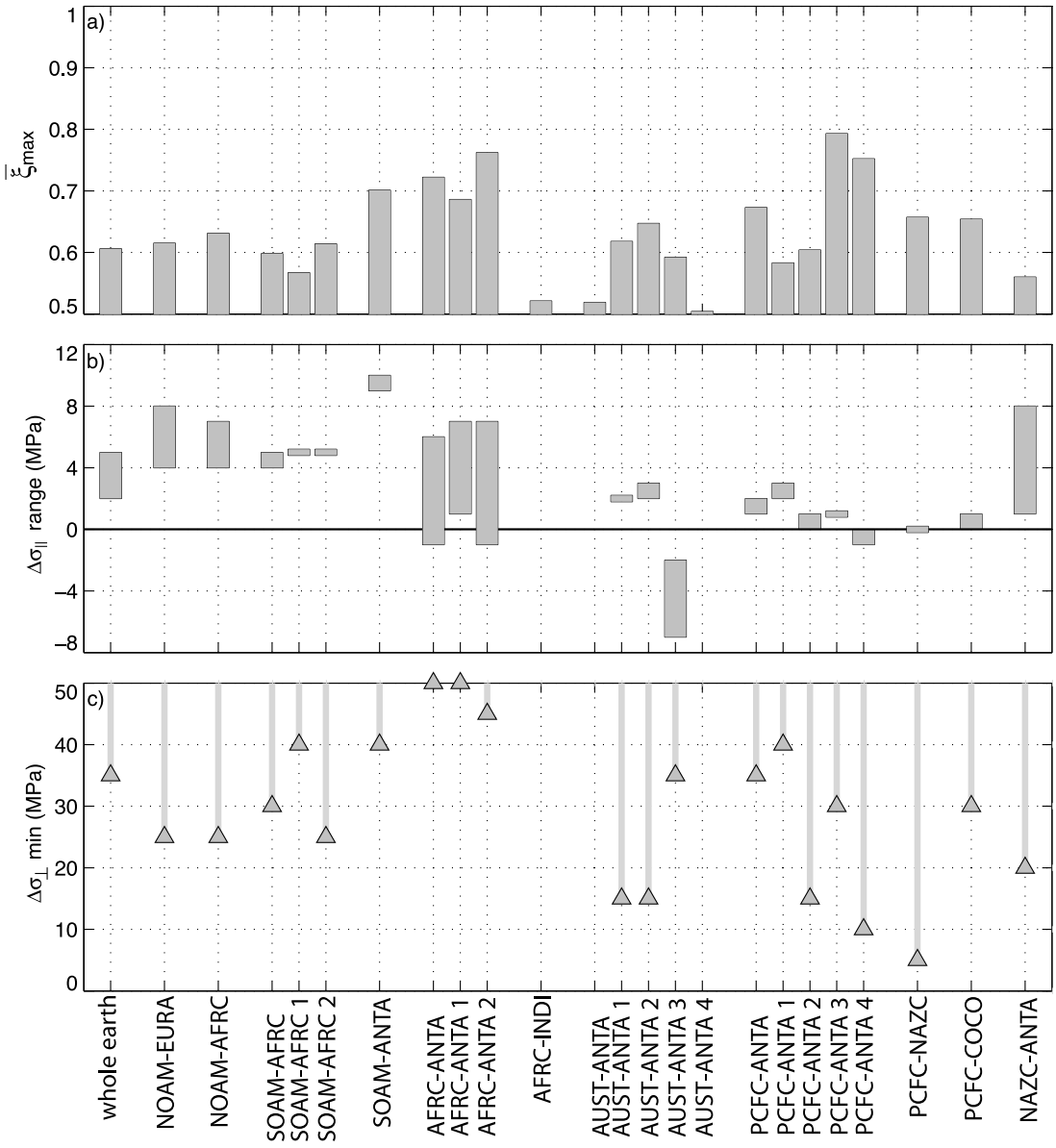

Figure 7. Summary of regional variation of (a) $\bar{\xi}_{max}$, (b) long-wavelength ridge-parallel stress ($\Delta\sigma_{\parallel}$) range, and (c) minimum ridge-perpendicular stress ($\Delta\sigma_{\perp}$). (Values are given in Table 3.) Values of $\Delta\sigma_{\parallel}$ and $\Delta\sigma_{\perp}$ are not shown for AFRC-INDI, AUST-ANTA, and AUST-ANTA 4 (regions 7, 8, and 8d) because these regions with $\bar{\xi}_{max} < 0.550$ are poorly constrained.

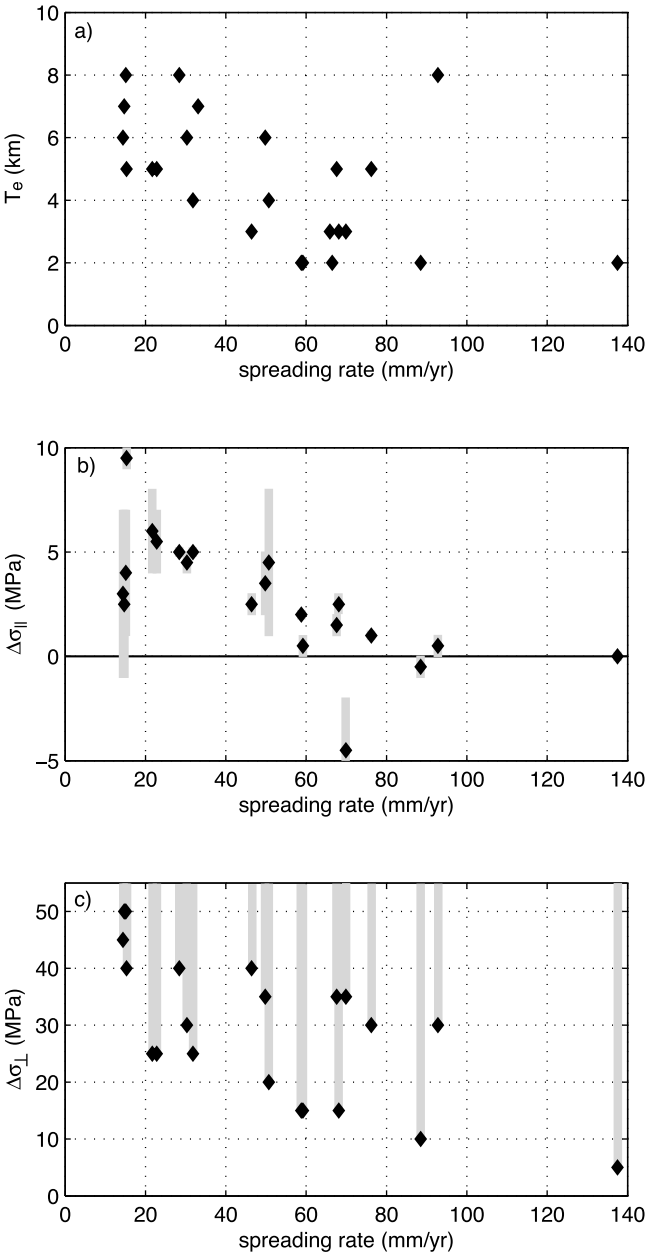

Figure 8. Spreading rate versus (a) elastic thickness, (b) range of ridge-parallel stress ($\Delta\sigma_{\parallel}$), and (c) minimum ridge-perpendicular stress ($\Delta\sigma_{\perp}$), for each plate boundary and subregion. (Values are given in Tables 1 and 3.) The value of $\Delta\sigma_{\parallel}$ plotted in Figure 8b is the midpoint of the acceptable range.

orientation of these transform segments is primarily defined by the preexisting need to connect the broken ends of the spreading axis, forcing the fault to be aligned with principal extension in the ridge-perpendicular direction. This observation agrees with previous studies suggesting that oceanic transform faults sustain very low shear stresses and may be poorly seismically coupled [e.g., *Behn et al.*, 2002; *Hall and Gurnis*, 2005].

[32] A curious result is that the discordant zone of the Australian-Antarctic plate boundary seems to require ridge-parallel compression in order to simultaneously fit the stress regime at both ridges and transforms. An alternative interpretation of this constraint is that the ridges require large ridge-parallel extension (15 MPa or more, see blue line of Figure 5 for region 8c) in order to bring even the ridges into a normal stress regime. With this much ridge-parallel extension, none of the transforms would remain in a strike-slip regime. This model result is likely a reflection of the anomalously low bathymetry in this region [e.g., *Forsyth et al.*, 1987; *Holmes et al.*, 2010], related to an anomalously low temperature and magma supply.

[33] The regions of AFRC-INDI, AUST-ANTA, and subregion AUST-ANTA 4 are the locations where the predictions of this model are least successful. These subregions make up a long section of ridge in the eastern Indian Ocean spreading at an intermediate rate. Model indications suggest that ridges at AFRC-INDI require nonzero ridge-parallel extension, but that transforms at this plate boundary require nonzero ridge-parallel compression. These two noncompatible conditions may reflect the presence of lower ridge topography with a deep axial valley in the northern section of this plate boundary contrasted with rugged topography with densely spaced fracture zones in the southern section. Model results at AUST-ANTA may also be divided into two sections by the slope of $\bar{\xi}_{ridge}$ as a function of $\Delta\sigma_{\parallel}$ (Figure 5). The western half (regions 8a and 8b) requires the ridge-parallel extension (or compression) to be near zero in order to fit both the ridges and transforms. The eastern half (regions 8c and 8d), including the discordant zone, exhibits a much shallower slope of $\bar{\xi}_{ridge}$, requiring a much higher extension in order to fit all the ridge points, but also allowing many of the ridge points to be fit even with ridge-parallel compression. This is principally indicative of the great variety of ridge-transform morphology along this plate boundary.

6. Conclusions

[34] We have demonstrated that the rapid variation in stress regime between spreading ridge and transform segments may be forward modeled as the sum of two stresses: a long-wavelength regionally uniform tectonic driving stress and a short-wavelength regionally varying stress related to the support of observable bathymetric features. The short-wavelength stress variations may be calculated as those of the critical elastic-plastic failure transition, measured by the second invariant of the deviatoric stress. This plastic failure stress ranges from ~0–70 MPa, depending on the ruggedness of the bathymetry. Along most spreading plate boundaries, we are able to satisfactorily model the observed variations in stress regime between normal ridges and strike-slip transforms. This suggests that short-wavelength bathymetry features, particularly a transform valley that is deeper than the nearby ridge axis topography, may be a necessary feature for the long-term endurance of an oceanic transform fault.

[35] We further use the calculations of the short-wavelength component to place constraints on the 2-D long-wavelength plate driving stress, and thus on the total in situ stress tensor. We find that ridge-perpendicular stress globally must exceed the sustained critical yield stress of deformation by at least 10–30 MPa of extensional stress along fast spreading ridges, 25–40 MPa extensional stress along slow

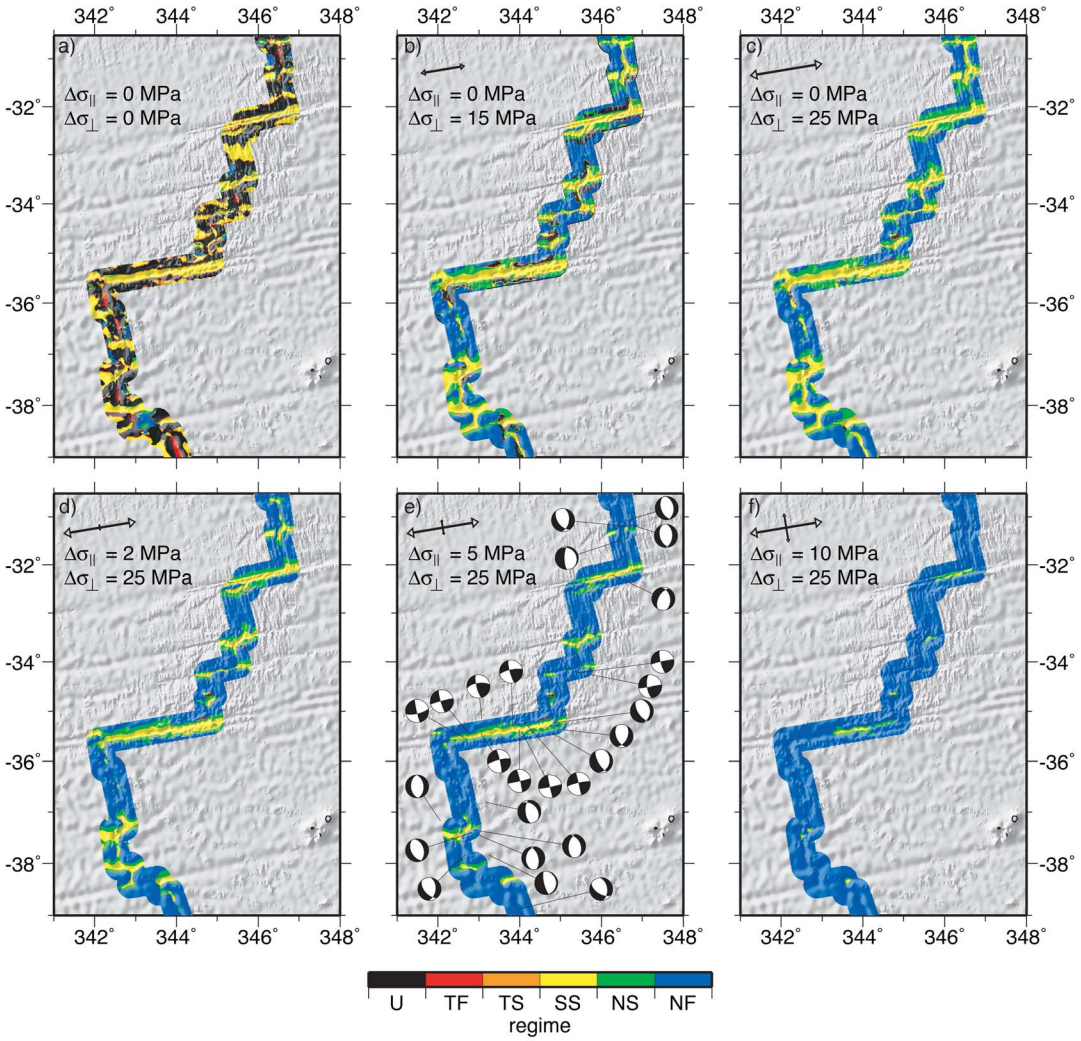

Figure 9. Spatial distribution of stress regime for topographic stress variations added to various long-wavelength stress fields, for the same area as shown in Figure 3. Thrust, strike-slip, and normal regime indicated by red, yellow, and blue, respectively. Oblique thrust and oblique normal regime indicated by orange and green, respectively. Black regions indicate the regime of the stress orientation is undefined. (Regime definition criteria are summarized in Table 2.) (a) Stress regime from short-wavelength topography alone with no additional long-wavelength stress. Stress regime with (b) insufficient $\Delta\sigma_\perp$ (15 MPa) and (c) minimum sufficient $\Delta\sigma_\perp$ (25 MPa). Stress regime with minimum sufficient $\Delta\sigma_\perp$ and (d) too little $\Delta\sigma_\parallel$ (2 MPa), (e) optimal $\Delta\sigma_\parallel$ (5 MPa), and (f) too much $\Delta\sigma_\parallel$ (10 MPa). WSM focal mechanisms shown atop best-fitting total stress field in Figure 9e with strike-slip regime predicted at low transform offsets and normal regime predicted nearly everywhere else.

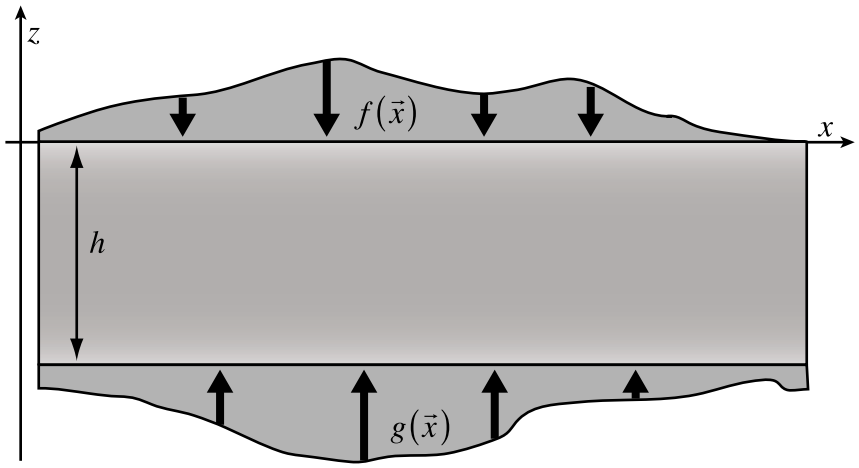

Figure A1. Schematic of elastic plate with thickness h with arbitrarily shaped nonidentical loads at the surface $f(\vec{x})$ and base $g(\vec{x})$.

spreading ridges, and 40–50 MPa extensional stress along ultra–slow spreading ridges. Additionally, we determine that ridge-parallel stress along fast spreading segments must be near zero, between 1 MPa compressional and 3 MPa extensional stress. Ridge-parallel stress along slow segments must be between 4 and 8 MPa extensional stress, and ridge-parallel stress along ultraslow segments must be between 1 MPa compressional and 7 MPa extensional stress.

Appendix A: Calculation of 3-D Stress in a Thick Elastic Plate

[36] The 3-D stress throughout a loaded thick elastic plate may be calculated semianalytically by numerically convolving the 2-D shape of the surface and base loads with an analytically calculated Green's function response of a thick elastic plate to nonidentical point loads. For the full derivation of this Green's function, see the appendix of *Luttrell et al.* [2011]. The solution is summarized here.

[37] Given an arbitrary surface load $f(x, y)$ at $z = 0$ and an arbitrary Moho load $g(x, y)$ at depth $z = h$ loading an elastic plate (Figure A1), the six components of the stress tensor can be calculated in the Fourier domain by

$$\sigma_{xx}(k_x,k_y,z) = f(\vec{k})\left[\frac{{k_x}^2}{|\vec{k}|^2}(C_f - S_f) - 2\nu S_f\frac{k_y^2}{|\vec{k}|^2}\right] + g(\vec{k})\left[\frac{{k_x}^2}{|\vec{k}|^2}(C_g - S_g) - 2\nu S_g\frac{k_y^2}{|\vec{k}|^2}\right], \quad \text{(A1)}$$

$$\sigma_{yy}(k_x,k_y,z) = f(\vec{k})\left[\frac{k_y^2}{|\vec{k}|^2}(C_f - S_f) - 2\nu S_f\frac{k_x^2}{|\vec{k}|^2}\right] + g(\vec{k})\left[\frac{k_y^2}{|\vec{k}|^2}(C_g - S_g) - 2\nu S_g\frac{k_x^2}{|\vec{k}|^2}\right], \quad \text{(A2)}$$

$$\sigma_{zz}(k_x,k_y,z) = f(\vec{k})\left[-C_f - S_f\right] + g(\vec{k})\left[-C_g - S_g\right], \quad \text{(A3)}$$

$$\sigma_{xy}(k_x,k_y,z) = \frac{k_x k_y}{|\vec{k}|^2}\{f(\vec{k})\left[C_f - S_f + 2\nu S_f\right] + g(\vec{k})\left[C_g - S_g + 2\nu S_g\right]\}, \quad \text{(A4)}$$

$$\sigma_{xz}(k_x,k_y,z) = \frac{ik_x}{|\vec{k}|}\left[f(\vec{k})S'_f + g(\vec{k})S'_g\right], \quad \text{(A5)}$$

$$\sigma_{yz}(k_x,k_y,z) = \frac{ik_y}{|\vec{k}|}\left[f(\vec{k})S'_f + g(\vec{k})S'_g\right], \quad \text{(A6)}$$

where $\vec{k} = (k_x, k_y)$ is the horizontal wave number and ν is Poisson's ratio. Note that the calculated stress will be physically unreasonable unless $f(\vec{k}) = g(\vec{k})$ at long wavelengths. The exact match between f and g is provided in the flexural equation (equation (B3)). Depth dependence for the normal stress components and the horizontal shear stress component is given by the transfer functions

$$C_f = \frac{2\beta^2 h\zeta\cosh\beta z - \beta z\sinh\beta z - \beta z\sinh\beta(h+\zeta)}{1 + 2\beta^2 h^2 - \cosh 2\beta h}, \quad \text{(A7)}$$

$$C_g = \frac{2\beta^2 hz\cosh\beta\zeta - \beta\zeta\sinh\beta\zeta - \beta\zeta\sinh\beta(h+z)}{1 + 2\beta^2 h^2 - \cosh 2\beta h}, \quad \text{(A8)}$$

$$S_f = \frac{2\beta h\sinh\beta z + \cosh\beta z - \cosh\beta(h+\zeta)}{1 + 2\beta^2 h^2 - \cosh 2\beta h}, \quad \text{(A9)}$$

$$S_g = \frac{2\beta h\sinh\beta\zeta + \cosh\beta\zeta - \cosh\beta(h+z)}{1 + 2\beta^2 h^2 - \cosh 2\beta h}, \quad \text{(A10)}$$

where $\beta = 2\pi|\vec{k}|$ is the radial wave number, z is the depth from the top of the plate, and $\zeta = h - z$ is the distance from the bottom of the plate. The two transfer functions related to the bottom load $g(\vec{k})$ are depth-inverted versions of those related to the top load $f(\vec{k})$, such that any occurrence of z and ζ are interchanged. The transfer functions for the vertical shear stress components are related to those in equations (A7)–(A10) by derivatives with respect to depth, such that

$$S'_{(f,g)} = -\frac{1}{\beta}\frac{d}{dz}\left[C_{(f,g)} + S_{(f,g)}\right]. \quad \text{(A11)}$$

[38] These solutions reduce to those of *Love* [1929] in the elastic half space limit at short wavelengths and match the 2-D solutions in the long wavelength limit as $\beta \to 0$ [*Luttrell et al.*, 2011].

[39] Equations (A1)–(A6) serve as Green's functions allowing the full 3-D stress tensor to be computed by a simple convolution in the Fourier domain. The second invariant of the deviatoric stress tensor $\tau_{ij} = \sigma_{ij} - \frac{1}{3}\sigma_{kk}$ is given by

$$II_\tau = \frac{1}{6}\left[\left(\sigma_{xx} - \sigma_{yy}\right)^2 + \left(\sigma_{xx} - \sigma_{zz}\right)^2 + \left(\sigma_{yy} - \sigma_{zz}\right)^2\right] + \sigma_{xy}^2 + \sigma_{xz}^2 + \sigma_{yz}^2. \tag{A12}$$

In terms of the transfer functions (A7)–(A11), this becomes

$$II_\tau = \frac{1}{3}\left[\begin{array}{l} 3\left(f\left(\vec{k}\right)C_f + g\left(\vec{k}\right)C_g\right)^2 - 3\left(f\left(\vec{k}\right)S'_f + g\left(\vec{k}\right)S'_g\right)^2 \\ +\left(f\left(\vec{k}\right)S_f + g\left(\vec{k}\right)S_g\right)^2(1-2\nu)^2 \end{array}\right], \tag{A13}$$

which is minimized when $\nu = \frac{1}{2}$, corresponding to an incompressible elastic solid. *Dahlen* [1981] similarly showed that in the two-dimensional case, the second invariant of the deviatoric stress from Airy compensated topography at mid-ocean ridges was minimized for $\nu = \frac{1}{2}$, though this was never explicitly stated. Our analysis extends the results of *Dahlen* [1981] to three dimensions.

Appendix B: Gravity Analysis

[40] Calculation of the stress state sustaining short-wavelength bathymetry variations requires both observations of the surface bathymetry, from satellite and ship tracks [*Becker et al.*, 2009], and an estimate of the buoyant load acting at the base of the finite-thickness elastic plate. This buoyancy may be derived from heterogeneities in either thermal structure or composition, either of which results in a density anomaly indicated in observations of gravity [*Sandwell and Smith*, 2009]. We use these gravity observations to determine a reasonable structure for the shape of the buoyant load at the base of the lithosphere [e.g., *Watts*, 2001]. We model the shape of the buoyant load as a filtered version of the surface load, with support of the surface topography coming from a combination of Airy compensation and the flexural strength of the elastic plate, effectively tuning the shape of the Moho with the elastic thickness of the crust.

[41] We calculate the gravity anomaly using the first term of the gravity expansion of *Parker* [1972] for a homogeneous single-layer crust of density ρ_c overlying a homogenous mantle of density ρ_m such that the total anomaly $g_{total} = g_{surface} + g_{Moho}$. The gravity anomaly at the surface, $z = z_s$, is given by [e.g., *Watts*, 2001]

$$g_{surface} = f_{topo} G \rho_c e^{-\beta(aobs - zs)}, \tag{B1}$$

where G is the gravitational constant, f_{topo} is the load of equivalent-rock topography (accounting for the overlying ocean mass), a_{obs} is the altitude of observation (in this case, the sea surface at $z = 0$), and $\beta = 2\pi\left|\vec{k}\right|$ is the radial wave number. The gravity anomaly at the Moho, $z = h + z_s$, is given by

$$g_{Moho} = f_{topo} G(\rho_c - \rho_m)\Phi e^{-\beta(aobs - h - zs)}, \tag{B2}$$

where the transfer function Φ is given by

$$\Phi = \frac{-\rho_c}{\rho_m - \rho_c}\left[1 + \frac{D\beta^4}{g(\rho_m - \rho_c)}\right]^{-1}, \tag{B3}$$

where g is the mean surface gravity, and the flexural rigidity D depends on the elastic thickness T_e, Young's modulus E, and Poisson's ratio ν as

$$D = \frac{E{T_e}^3}{12(1-\nu)}. \tag{B4}$$

[42] For our gravity calculations, we use a mean ocean depth of z_s = 3 km, a mantle density of 3300 kg/m^3, a Young's modulus of 70 GPa, and a Poisson's ratio of 0.5. Because the variation in ocean ridge depth about z_s is much less than the value of z_s, using a single ocean depth value is a very good approximation for all but the shortest wavelengths (<2 km), as this value only acts as an attenuation distance. For the quantity of water mass overlying the seafloor, the actual bathymetry is used. The choice of Poisson's ratio is made to be consistent with the stress calculations of this study (Appendix A) and has little impact on the gravity analysis, as it only appears within the flexural rigidity such that the difference in gravity anomaly of a material with ν = 0.25 and ν = 0.5 is about 7%. There are two parameters that we allow to vary: the density and elastic thickness of the crust. We use a crustal thickness of 6.5 km (G. Laske et al., CRUST 2.0: A new global crustal model at 2x2 degrees, 2001, http://igppweb.ucsd.edu/~gabi/rem.html), recognizing that the gravity-topography transfer function is relatively insensitive to crustal thickness at the short wavelengths considered here.

[43] We calculate the global gravity field for a crustal density between 2400–3000 kg/m^3 and elastic thickness between 0–20 km. We then compare the model with the high-pass-filtered gravity data only at points where the bathymetry data are from ship soundings and that are within 30 km either side of the ridge or transform segment [*Sandwell and Smith*, 2009]. These precautions ensure that our analysis is focused on the plate boundary and that the observed and model gravity are largely derived from independent data. We then calculate the RMS misfit, defined as

$$RMS = \sqrt{\frac{\sum_{i=1}^{N}\left(g_i^{observation} - g_i^{model}\right)^2}{N}}, \tag{B5}$$

for the global mid-ocean ridge and for each plate boundary separately (Figure 2), and determine the best fitting values of crustal density and elastic thickness (Table 1 and Figure B1). As usual, we find there is a tradeoff to gravity fit between density and elastic thickness. Though the strict minimum RMS often corresponds to the highest considered density (3000 kg/m^3), we find the difference in RMS from a density of 2800 kg/m^3 is negligible and select this as our preferred crustal density.

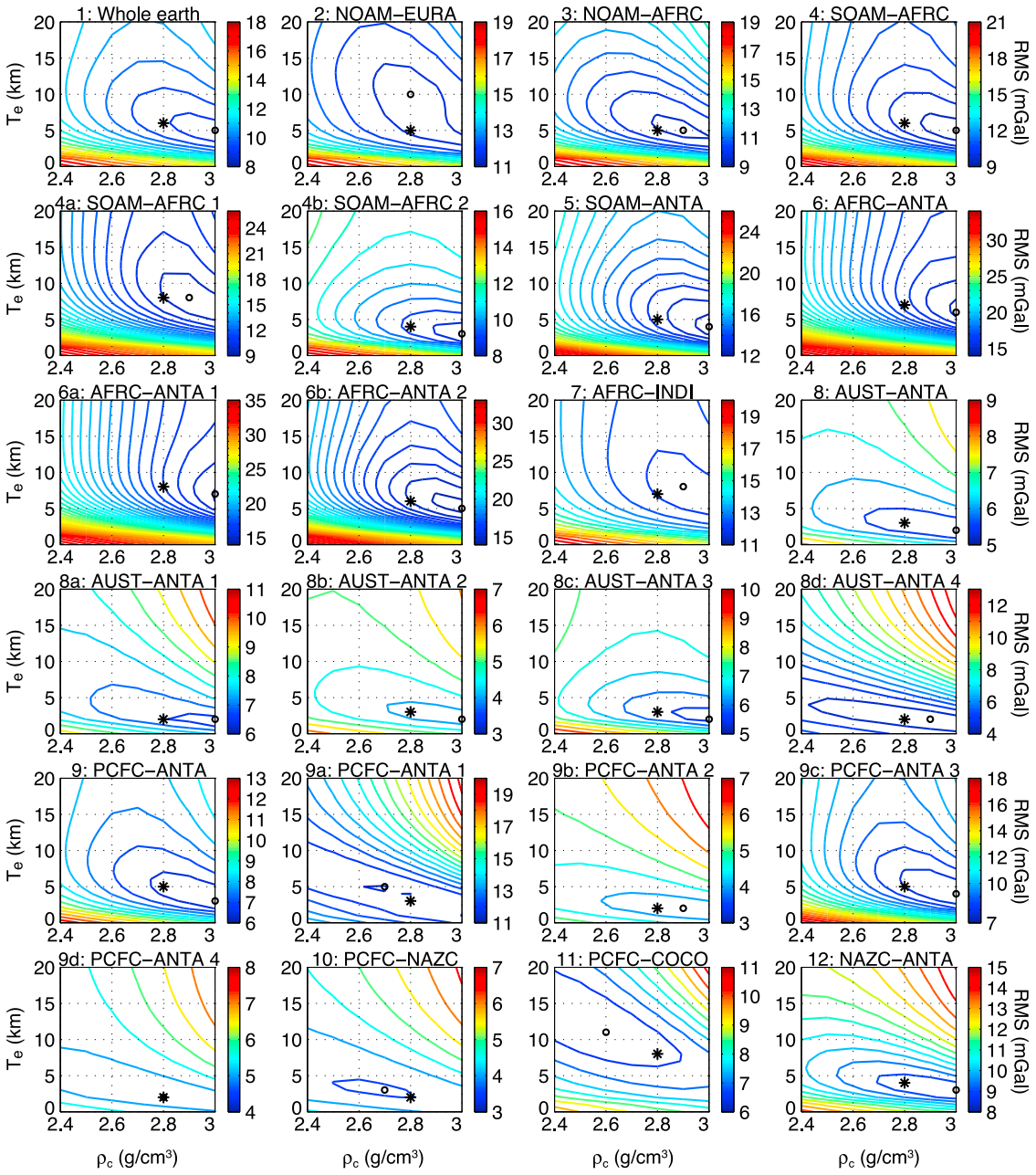

Figure B1. Contours of RMS misfit between gravity model and data for each plate boundary and subregion as a function of crustal density and elastic thickness. Contour interval is 0.5 mGal. Black circle indicates the absolute lowest RMS value. Black star indicates best model with crustal density 2800 kg/m^3. Optimal parameters for each region and their corresponding RMS values are listed in Table 1.

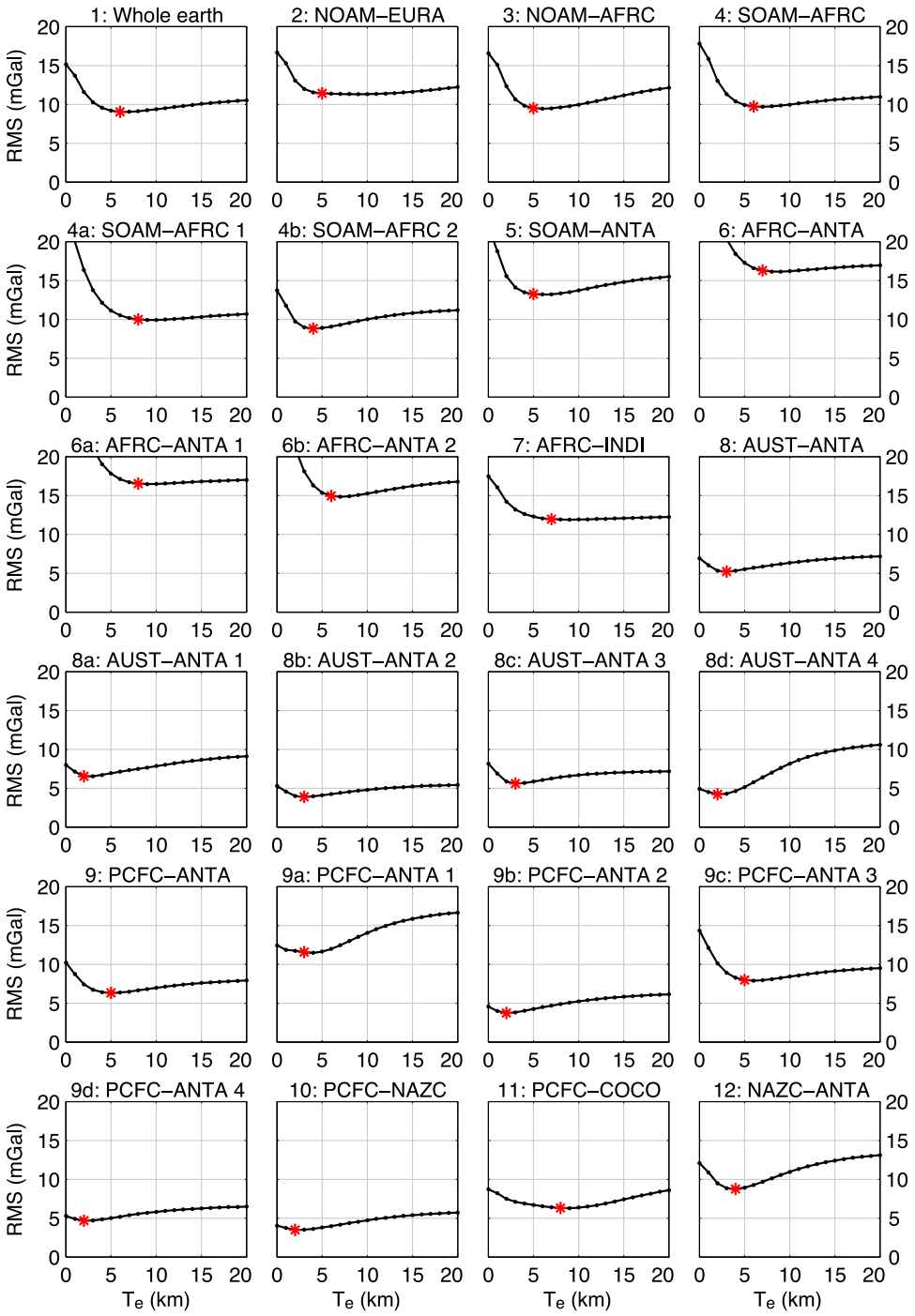

Figure B2. RMS misfit between gravity model and data for each plate boundary and subregion as a function of elastic thickness, assuming a crustal density of 2800 kg/m^3. Red star indicates lowest elastic thickness value that minimizes RMS.

[44] We then determine the most suitable elastic thickness for each region (Figure B2). In regions where the minimum RMS is broad and spans several elastic thickness values, we select the smallest suitable value. Generally the optimal elastic thickness ranges from 2–8 km. The fast spreading sections of the mid-ocean ridge in the Pacific Ocean require a smaller elastic thickness of 2 km, while the slower spreading sections of the mid-Atlantic Ocean are fit with a higher elastic thickness, ~5 km. The ultraslow boundaries in the southwestern Indian Ocean are strongest, with a best elastic thickness of 7 km. These values generally agree with those of *Cochran* [1979], who found gravity profiles across the mid-Atlantic ridge to be best fit with a crustal density of 2600 kg/m^3 and an elastic thickness of 9 km, while profiles across the East Pacific Rise required a smaller elastic thickness. At plate boundaries NOAM-EURA, SOAM-ANTA, AUST-ANTA 4, and PCFC-ANTA 1 (regions 2, 5, 8d, and 9a), the constrained gravity observations are particularly

sparse. However, the optimized parameters from these limited data are consistent with those of neighboring regions, so we use these parameters without additional correction.

[45] **Acknowledgments.** We thank Kaj Johnson and an anonymous reviewer for their helpful comments on the manuscript. This research was supported by the NASA Earth and Space Science Fellowship Program, by NSF EAR0811772, and partly by the NSF Marine Geology and Geophysics Program OCE0825045.

References

Becker, J. J., et al. (2009), Global bathymetry and elevation data at 30 arc seconds resolution: SRTM30_PLUS, *Mar. Geod.*, *32*(4), 355–371, doi:10.1080/01490410903297766.

Behn, M. D., J. Lin, and M. T. Zuber (2002), Evidence for weak oceanic transform faults, *Geophys. Res. Lett.*, *29*(24), 2207, doi:10.1029/2002GL015612.

Blackman, D. K., and D. W. Forsyth (1989), Axial topographic relief associated with ridge transform intersections, *Earth Planet. Sci. Lett.*, *95*(1–2), 115–129, doi:10.1016/0012-821X(89)90171-4.

Buck, W. R., L. L. Lavier, and A. N. B. Poliakov (2005), Modes of faulting at mid-ocean ridges, *Nature*, *434*(7034), 719–723, doi:10.1038/nature03358.

Chen, Y. J. (1992), Oceanic crustal thickness versus spreading rate, *Geophys. Res. Lett.*, *19*(8), 753–756, doi:10.1029/92GL00161.

Chen, Y. J. (1996), Dynamics of the mid-ocean ridge plate boundary: Recent observations and theory, *Pure Appl. Geophys.*, *146*(3–4), 621–648, doi:10.1007/BF00874736.

Chen, Y., and W. J. Morgan (1990), Rift valley/no rift valley transition at mid-ocean ridges, *J. Geophys. Res.*, *95*(B11), 17,571–17,581, doi:10.1029/JB095iB11p17571.

Choi, E. S., L. Lavier, and M. Gurnis (2008), Thermomechanics of mid-ocean ridge segmentation, *Phys. Earth Planet. Inter.*, *171*(1–4), 374–386, doi:10.1016/j.pepi.2008.08.010.

Coblentz, D. D., R. M. Richardson, and M. Sandiford (1994), On the gravitational potential of the Earth's lithosphere, *Tectonics*, *13*(4), 929–945, doi:10.1029/94TC01033.

Cochran, J. R. (1979), Analysis of isostasy in the world's oceans: 2. Midocean ridge crests, *J. Geophys. Res.*, *84*(B9), 4713–4729, doi:10.1029/JB084iB09p04713.

Collette, B. J. (1974), Thermal contraction joints in a spreading seafloor as origin of fracture zones, *Nature*, *251*(5473), 299–300, doi:10.1038/251299a0.

Crawford, W. C., S. C. Webb, and J. A. Hildebrand (1998), Estimating shear velocities in the oceanic crust from compliance measurements by two-dimensional finite difference modeling, *J. Geophys. Res.*, *103*(B5), 9895–9916, doi:10.1029/97JB03532.

Dahlen, F. A. (1981), Isostasy and the ambient state of stress in the oceanic lithosphere, *J. Geophys. Res.*, *86*(B9), 7801–7807, doi:10.1029/JB086iB09p07801.

DeMets, C., R. G. Gordon, and D. F. Argus (2010), Geologically current plate motions, *Geophys. J. Int.*, *181*(1), 1–80, doi:10.1111/j.1365-246X.2009.04491.x.

Dick, H. J. B., J. Lin, and H. Schouten (2003), An ultraslow-spreading class of ocean ridge, *Nature*, *426*(6965), 405–412, doi:10.1038/nature02128.

Forsyth, D. W., R. L. Ehrenbard, and S. Chapin (1987), Anomalous upper mantle beneath the Australian-Antarctic discordance, *Earth Planet. Sci. Lett.*, *84*(4), 471–478, doi:10.1016/0012-821X(87)90011-2.

Fox, P. J., and D. G. Gallo (1984), A tectonic model for ridge-transform-ridge plate boundaries: Implications for the structure of oceanic lithosphere, *Tectonophysics*, *104*(3–4), 205–242, doi:10.1016/0040-1951(84)90124-0.

Gerya, T. (2010), Dynamical instability produces transform faults at mid-ocean ridges, *Science*, *329*(5995), 1047–1050, doi:10.1126/science.1191349.

Ghosh, A., W. E. Holt, and L. M. Flesch (2009), Contribution of gravitational potential energy differences to the global stress field, *Geophys. J. Int.*, *179*(2), 787–812, doi:10.1111/j.1365-246X.2009.04326.x.

Gregg, P. M., J. Lin, M. D. Behn, and L. G. J. Montesi (2007), Spreading rate dependence of gravity anomalies along oceanic transform faults, *Nature*, *448*(7150), 183–187, doi:10.1038/nature05962.

Grindlay, N. R., and P. J. Fox (1993), Lithospheric stresses associated with nontransform offsets of the Mid-Atlantic Ridge: Implications from a finite-element analysis, *Tectonics*, *12*(4), 982–1003, doi:10.1029/93TC00364.

Gudmundsson, A. (1995), Stress fields associated with oceanic transform faults, *Earth Planet. Sci. Lett.*, *136*(3–4), 603–614, doi:10.1016/0012-821X(95)00164-8.

Hall, C. E., and M. Gurnis (2005), Strength of fracture zones from their bathymetric and gravitational evolution, *J. Geophys. Res.*, *110*, B01402, doi:10.1029/2004JB003312.

Heidbach, O., M. Tingay, A. Barth, J. Reinecker, D. Kurfeß, and B. Müller (2008), The World Stress Map database release 2008, http://dc-app3-14.gfz-potsdam.de/pub/poster/World_Stress_Map_Release_2008.pdf, GFZ German Res. Cent. for Geosci., Potsdam, Germany, doi:10.1594/GFZ.WSM.Rel2008.

Hieronymus, C. F. (2004), Control on seafloor spreading geometries by stress- and strain-induced lithospheric weakening, *Earth Planet. Sci. Lett.*, *222*(1), 177–189, doi:10.1016/j.epsl.2004.02.022.

Holmes, R. C., M. Tolstoy, A. J. Harding, J. A. Orcutt, and J. P. Morgan (2010), Australian Antarctic Discordance as a simple mantle boundary, *Geophys. Res. Lett.*, *37*, L09309, doi:10.1029/2010GL042621.

Love, A. E. H. (1929), The stress produced in a semi-infinite solid by pressure on part of the boundary, *Proc. R. Soc. London, A*, *228*, 377–420.

Luttrell, K., X. Tong, D. Sandwell, B. Brooks, and M. Bevis (2011), Estimates of stress drop and crustal tectonic stress from the 27 February 2010 Maule, Chile earthquake: Implications for fault strength, *J. Geophys. Res.*, *116*, B11401, doi:10.1029/2011JB008509.

Macdonald, K. C. (1982), Mid-ocean ridges: Fine scale tectonic, volcanic and hydrothermal processes within the plate boundary zone, *Annu. Rev. Earth Planet. Sci.*, *10*, 155–190, doi:10.1146/annurev.ea.10.050182.001103.

Macdonald, K. C., P. J. Fox, R. T. Alexander, R. Pockalny, and P. Gente (1996), Volcanic growth faults and the origin of Pacific abyssal hills, *Nature*, *380*(6570), 125–129, doi:10.1038/380125a0.

Martel, S. J., and J. R. Muller (2000), A two-dimensional boundary element method for calculating elastic gravitational stresses in slopes, *Pure Appl. Geophys.*, *157*(6–8), 989–1007, doi:10.1007/s000240050014.

Menard, H. W. (1984), Evolution of ridges by asymmetrical spreading, *Geology*, *12*(3), 177–180, doi:10.1130/0091-7613(1984)12<177:EORBAS>2.0.CO;2.

Neves, M. C., M. H. P. Bott, and R. C. Searle (2004), Patterns of stress at midocean ridges and their offsets due to seafloor subsidence, *Tectonophysics*, *386*(3–4), 223–242, doi:10.1016/j.tecto.2004.06.010.

Oldenburg, D. W., and J. N. Brune (1972), Ridge transform fault spreading pattern in freezing wax, *Science*, *178*(4058), 301–304, doi:10.1126/science.178.4058.301.

Pan, J. F., M. Antolik, and A. M. Dziewonski (2002), Locations of mid-oceanic earthquakes constrained by seafloor bathymetry, *J. Geophys. Res.*, *107*(B11), 2310, doi:10.1029/2001JB001588.

Parker, R. L. (1972), Rapid calculation of potential anomalies, *Geophys. J. R. Astron. Soc.*, *31*(4), 447–455.

Phipps Morgan, J., and E. M. Parmentier (1984), Lithospheric stress near a ridge-transform intersection, *Geophys. Res. Lett.*, *11*(2), 113–116, doi:10.1029/GL011i002p00113.

Pockalny, R. A., P. Gente, and R. Buck (1996), Oceanic transverse ridges: A flexural response to fracture-zone-normal extension, *Geology*, *24*(1), 71–74, doi:10.1130/0091-7613(1996)024<0071:OTRAFR>2.3.CO;2.

Purdy, G. M., L. S. L. Kong, G. L. Christeson, and S. C. Solomon (1992), Relationship between spreading rate and the seismic structure of midocean ridges, *Nature*, *355*(6363), 815–817, doi:10.1038/355815a0.

Sandwell, D. T. (1986), Thermal-stress and the spacings of transform faults, *J. Geophys. Res.*, *91*(B6), 6405–6417, doi:10.1029/JB091iB06p06405.

Sandwell, D. T., and W. H. F. Smith (2009), Global marine gravity from retracked Geosat and ERS-1 altimetry: Ridge segmentation versus spreading rate, *J. Geophys. Res.*, *114*, B01411, doi:10.1029/2008JB006008.

Small, C., and D. T. Sandwell (1994), Imaging midocean ridge transitions with satellite gravity, *Geology*, *22*(2), 123–126, doi:10.1130/0091-7613(1994)022<0123:IMORTW>2.3.CO;2.

Smith, W. H. F., and D. T. Sandwell (1997), Global sea floor topography from satellite altimetry and ship depth soundings, *Science*, *277*(5334), 1956–1962, doi:10.1126/science.277.5334.1956.

Watts, A. B. (2001), *Isostasy and Flexure of the Lithosphere*, Cambridge Univ. Press, Cambridge, U. K.

Zoback, M. L. (1992), First- and second-order patterns of stress in the lithosphere: The World Stress Map project, *J. Geophys. Res.*, *97*(B8), 11,703–11,728, doi:10.1029/92JB00132.

K. Luttrell, Volcano Science Center, U.S. Geological Survey, 345 Middlefield Rd., MS 910, Menlo Park, CA 94025, USA. (kluttrell@usgs.gov)

D. Sandwell, Scripps Institution of Oceanography, University of California, San Diego, 9500 Gilman Dr., MS 225, La Jolla, CA 92093, USA. (dsandwell@ucsd.edu)